ASCE

Earthquake and Postearthquake Fire Testing of a Midrise Cold-Formed Steel-Framed Building. I: Building Response and Physical Damage

Tara C. Hutchinson, M.ASCE[1]; Xiang Wang[2]; Gilbert Hegemier[3]; Praveen Kamath[4]; and Brian Meacham[5]

Abstract: To advance understanding of the multihazard performance of midrise cold-formed steel (CFS) construction, a unique multidisciplinary experimental program was conducted on the Large High-Performance Outdoor Shake Table (LHPOST) at the University of California, San Diego (UCSD). The centerpiece of this project involved earthquake and live fire testing of a full-scale 6-story CFS wall braced building. Initially, the building was subjected to seven earthquake tests of increasing motion intensity, sequentially targeting service, design, and maximum credible earthquake (MCE) demands. Subsequently, live fire tests were conducted on the earthquake-damaged building at two select floors. Finally, for the first time, the test building was subjected to two postfire earthquake tests, including a low-amplitude aftershock and an extreme near-fault target MCE-scaled motion. In addition, low-amplitude white noise and ambient vibration data were collected during construction and seismic testing phases to support identification of the dynamic state of the building system. This paper offers an overview of this unique multihazard test program and presents the system-level structural responses and physical damage features of the test building throughout the earthquake-fire-earthquake test phases, whereas the component-level seismic behavior of the shear walls and seismic design implications of CFS-framed building systems are discussed in a companion paper. **DOI: 10.1061/(ASCE)ST.1943-541X.0003097.**

Author keywords: Cold-formed steel (CFS); Fire testing; Light-framed construction; Seismic performance; Shake-table testing.

Introduction

Growth in the use of cold-formed steel (CFS) framed construction in high seismic regions (e.g., the western US) has been substantial in recent years as a result of the advances related to the design guidelines for such light-framed structures (AISI 2015a, b; NIST 2016). Structural systems of this kind consist of repetitively framed wall-braced vertical structural elements fabricated using CFS framing members (e.g., studs, tracks, and joists) attached with sheathing materials (e.g., wood or sheet steel) as well as floor diaphragms constructed using similar framing and sheathing products as the horizontal structural elements. CFS has many natural benefits to offer when utilized as the primary load-resisting system in buildings. Among them, its high strength-to-weight ratio and inherent noncombustibility result in a material with the promise to offer resiliency following both earthquake and postearthquake fire hazard scenarios.

In the last few decades, experimental investigations have been devoted to advancing understanding regarding the seismic response of CFS-framed shear wall components. Notably, the work conducted by Serrette et al. (1997) represents one of the first efforts of its kind in North America to study the seismic response of CFS-framed shear walls. This effort largely formed the initial basis for codified design of CFS systems [e.g., AISI S240 (AISI 2015a); AISI S400 (AISI 2015b)]. Rogers and colleagues extended these and similar efforts to investigate CFS wall behavior with varied sheathing materials and framing details (e.g., Branston et al. 2006). Their experimental studies included pseudostatic tests of CFS-framed steel strap shear walls (Al-Kharat and Rogers 2007) and steel-sheet shear walls (Balh et al. 2014), as well as pseudodynamic tests of 2-story steel-sheet shear wall assemblies (Shamim et al. 2013).

In addition, recent experimental studies involved testing of CFS shear walls sheathed with sheet steel (Yu 2010), oriented strand board (OSB) panels (Liu et al. 2014), and corrugated steel (Zhang et al. 2016, 2017). Similar research has occurred outside of North America, including pseudostatic testing of wood-sheathed shear walls (Fülöp and Dubina 2004; Landolfo et al. 2006), strap-braced shear walls (Iuorio et al. 2014), gypsum-sheathed shear walls (Macillo et al. 2017), and multistory shear wall assemblies (Wang and Ye 2016). In contrast, experimental studies on the seismic behavior of CFS-framed structures configured in their system-level arrangement (i.e., building systems or subassemblies) have only occurred in a handful of shake-table experiments of CFS-framed buildings with three stories or less (e.g., Peterman et al. 2016a, b;

[1]Professor, Dept. of Structural Engineering, Univ. of California, San Diego, La Jolla, CA 92093-0085.

[2]Postdoctoral Researcher, Dept. of Structural Engineering, Univ. of California, San Diego, La Jolla, CA 92093-0085 (corresponding author). ORCID: https://orcid.org/0000-0002-9845-1875. Email: xiw002@eng.ucsd.edu

[3]Distinguished Professor (Emeritus), Dept. of Structural Engineering, Univ. of California, San Diego, La Jolla, CA 92093-0085.

[4]Fire Engineer, Holmes Fire LP, 2/414 Kent St., Sydney, NSW, Australia; formerly, Postdoctoral Researcher, Dept. of Fire Protection Engineering, Worcester Polytechnic Institute, Worcester, MA 01609.

[5]Managing Principal, Meacham Associates, 4 Woodchuck Hill Rd., Shrewsbury, MA 01545; formerly, Associate Professor, Dept. of Fire Protection Engineering, Worcester Polytechnic Institute, Worcester, MA 01609. ORCID: https://orcid.org/0000-0002-8562-3471

Note. This manuscript was submitted on June 18, 2020; approved on April 8, 2021; published online on June 28, 2021. Discussion period open until November 28, 2021; separate discussions must be submitted for individual papers. This paper is part of the ***Journal of Structural Engineering***, © ASCE, ISSN 0733-9445.

Fiorino et al. 2017, 2019). Nonetheless, there remains a paucity of experimental data to support understanding the seismic behavior of midrise CFS-framed buildings. Advancing knowledge in this regard is particularly pressing given that the height of these light-frame structures is allowed to reach as much as 18 m as per current design guidelines (ASCE 2016).

To address the need for understanding the earthquake and post-earthquake fire behavior of midrise CFS-framed buildings, a unique multidisciplinary test project was conducted on the Large High-Performance Outdoor Shake Table (LHPOST) at the University of California, San Diego (UCSD). Central to this research is the system-level earthquake and live fire testing of a full-scale 6-story CFS wall braced building. In a 3-week test program, this full-scale building was subjected to seven earthquake tests of increasing motion intensity. Earthquake motions were scaled to impose service, design, and maximum credible earthquake (MCE) demands onto the test building. Subsequently, live fire tests were conducted on the earthquake-damaged building at two select floors (Floors 2 and 6). Finally, the test building was subjected to two postfire earthquake tests, including a low-amplitude aftershock and an extreme near-fault target MCE intensity motion.

The experimental findings from this comprehensive test program are summarized in a series of two companion papers. In this companion paper series, the present (first) paper offers an overview of the earthquake-fire-earthquake test program and summarizes the system-level earthquake and fire responses of the test building as well as the associated physical damage features throughout the three phases of the multihazard test program, whereas the second paper discusses the seismic behavior of individual shear walls in the system-level tests and the ensuing implications related to the seismic design and analysis of CFS wall-framed structural systems (Wang and Hutchinson 2021).

Test Building Design and Construction

Test Building and Structural Design

A 6-story CFS test building (Fig. 1) was designed and erected on the LHPOST facility at UCSD (NHERI@UC San Diego). For the purposes of design, this test building was assumed to be located in a high seismic region near downtown Los Angeles, California, with its design basis complying with current code provisions within ASCE 7 (ASCE 2016), AISI S240 (AISI 2015a), and AISI S400 (AISI 2015b). For simplicity, a uniform plan with the dimension of 10.4 m (34 ft) × 7.3 m (24 ft) at each floor was adopted, allowing the specimen to nearly occupy the entire 12.2 m (40 ft) × 7.6 m (25 ft) shake-table footprint. The total height of the building was 19.2 m above the shake-table platen [floor-to-floor height of 3.1 m (10 ft) for all stories and a 1.2 m (4 ft) tall parapet on the roof perimeter]. The seismic design considered uniformly distributed dead and live loads of 1.5 kN/m^2 (32 psf) and 1.9 kN/m^2 (40 psf) at each floor, with the exception of an assumed live load on the roof of 1.0 kN/m^2 (20 psf). Consequently, the effective seismic design weight of the test building was assumed as 1,420 kN (320 kips).

According to ASCE 7 code provisions (ASCE 2016), the CFS wall braced building was designed with a response modification factor R of 6.5, an overstrength factor Ω of 3.0, and a deflection amplification factor C_d of 4.0. The code-based fundamental period of the test building T was determined as 0.43 s considering a total building height of 18.3 m (60 ft) excluding the parapets. The base shear coefficient C_s of the test building was consequently determined as 0.236, which resulted in an effective seismic design base shear V_b of 334 kN (75 kips). In addition, the weight of the test building (including its nonstructural components) was estimated

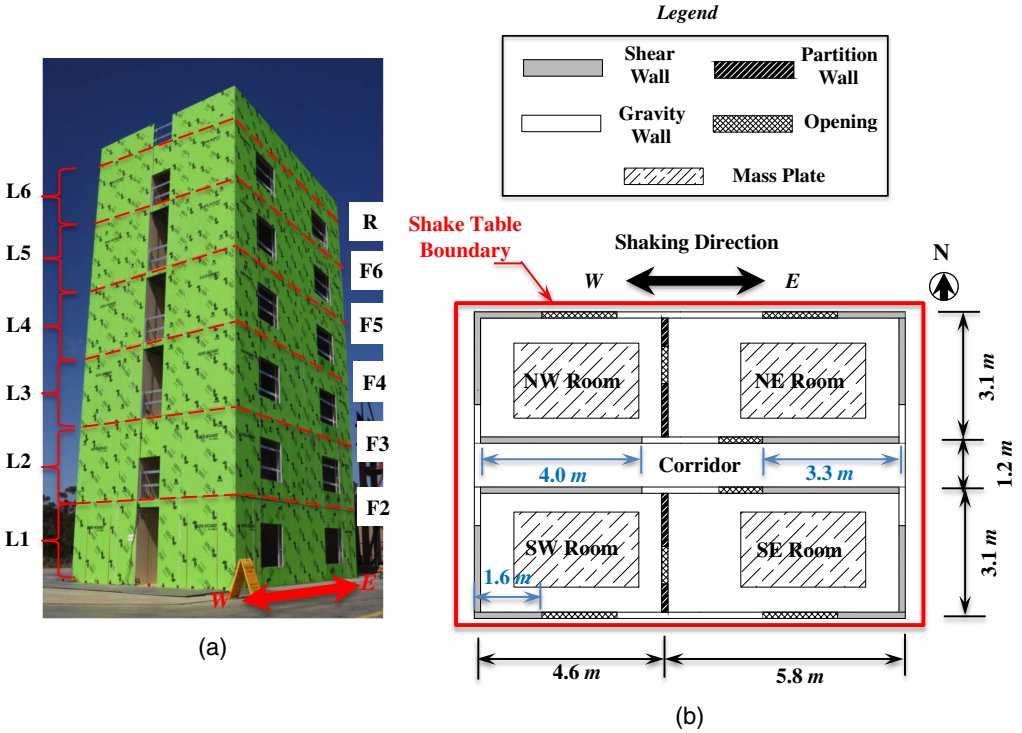

Fig. 1. Test building: (a) isometric view of the building (L# denotes level number and F# denotes floor number) (images by Xiang Wang); and (b) schematic building plan layout typical of Floors 2 to 6. Floor 1 is identical sans the absence of transverse partition walls and mass plates. Interior arrow annotations denote the lengths of longitudinal walls (1 m = 3.3 ft).

J. Struct. Eng., 2021, 147(9): 04021125

as 1,160 kN (260 kips) by averaging the measured vertical loads acting on the shake table during individual earthquake tests. The actual building weight was slightly lower than that considered in seismic design by ~260 kN (60 kips) to account for the reduction of live loads (reduction factor of ~0.6) in the event of an earthquake. The estimated maximum inelastic story drift of the building was ~1.0%, with a deflection amplification factor C_d of 4.0, which was lower than the allowable story drift of 2.0% as prescribed in ASCE 7 provisions (ASCE 2016).

The building had a symmetric floor plan with a corridor 1.2 m (4 ft) wide oriented along the longitudinal centerline [Fig. 1(b)]. Two transverse partition walls were located 0.6 m (2 ft) west of the transverse centerline (Level 2 through Level 6), each separating two rooms on the same side of the corridor. No partition walls were installed at the first level to simplify the attachment to the shake table. The exterior wall layout of the building resulted in four partial-height window openings (one at each room) and two full-height corridor openings (at each end of the corridor) at each level [Fig. 1(a)]. Dropped (partial height) soffits were constructed on the corridor openings at Level 2 and Level 6 to emulate ventilation conditions for the fire tests. To account for the live loads and the weight of certain architectural features excluded from construction (e.g., flooring and exterior façade finishing), four mass plates each with a weight of ~16.5 kN (3.7 kips) were installed on the floor diaphragm at each floor from the second floor through the roof [Fig. 1(b)].

Structural Systems (Walls and Diaphragms)

The test building was detailed to carry lateral seismic loads as a repetitively framed system using prefabricated CFS diaphragms and wall panels with the exception of the in situ fabrication of the wall system adopted at the first level. As illustrated in Fig. 1(b), two longitudinal shear walls were placed along each (east and west) end of the corridor, with an associated wall length of 4.0 m (13 ft) and 3.3 m (11 ft) for the walls at the west and east ends, respectively. In addition, short exterior shear walls with a length of ~1.6 m (5 ft 4 in.) in the longitudinal direction and ~2.1 m (7 ft) in the transverse direction were placed at the four corners of the building. The total shear wall length per floor was 21.3 m (70 ft) in the longitudinal (shaking) direction and 8.6 m (28 ft) in the transverse direction. The corridor shear walls were designed as the primary lateral-load-resisting elements in the direction of shaking, whereas the exterior (short) shear walls at the corners of the building were assumed to resist transverse and torsion loads during the tests. With the assumption that the design base shear was entirely resisted by the corridor shear walls, the nominal shear demand required of the first level corridor shear walls in the longitudinal shaking direction was 22.8 kN/m (1.6 kip/ft).

The shear walls were constructed using standard CFS framing members (e.g., studs and tracks) [Fig. 2(a)]. Sheathing materials utilized load-resisting structural panels on the exterior (or corridor) side and regular gypsum boards 16 mm (5/8 in.) thick on the interior (room) side. The structural panels were fabricated using 16 mm (5/8 in.) thick gypsum boards bonded with a layer of 0.686 mm (0.027 in.) thick (22 gauge) sheet steel to provide lateral resistance to the shear walls. The corridor shear walls were fabricated using vertical studs 600S200-68 at the first level and 600S200-54 at all remaining levels. All the framing studs were spaced at 610 mm (24 in.) on center (o.c.). The (top and bottom) tracks were consistently constructed using 600T200-54, with the exception of the 600T200-97 base tracks (bottom tracks of the first level shear walls).

In addition, the chord studs (in a double stud pattern) at the edge of the door and window openings were constructed using 600S200-68. The structural sheathing panels along the corridor walls were attached to framing using #8 self-tapping metal screws spaced at 406 mm (16 in.) o.c. in the field and varying boundary (edge) spacing of 76 mm (3 in.) o.c. for the lower three levels, 102 mm (4 in.) for Level 4, and 152 mm (6 in.) o.c. for the upper two levels. The details of the exterior shear walls were similar to those of the corridor shear walls, except (1) vertical studs utilized 600S200-54 at 610 mm (24 in.) o.c. at all levels, (2) structural panels utilized 16 mm (5/8 in.) thick moisture-resistant gypsum boards instead of regular gypsum boards because they were placed on the building exterior, and (3) screw spacing was 152 mm (6 in.) o.c. on the boundary and 406 mm (16 in.) o.c. in field at all levels.

Uniquely, this midrise test building adopted a pair of steel rod and compression stud assemblies embedded within each shear wall to resist tension and compression loads at the ends of the shear walls during lateral earthquake loading [Fig. 2(a)]. The assembly consisted of large-diameter steel rods that spanned continuously over the full height of the building as well as compression stud packs embedded with the repetitive shear wall framing at each level [Fig. 2(b)]. The capacity design concept was employed when detailing the compression stud packs and steel rods of the continuous tie-down assemblies. In compliance with ASCE 7 code provisions (ASCE 2016), an overstrength factor of 3.0 was adopted to implicitly consider the reserved strength of the shear walls and the additional lateral strength contribution from nondesignated structural components (e.g., gypsum panels and gravity walls). Further discussions of the tie-rod and compression stud pack assemblies and their seismic behavior have been given by Wang and Hutchinson (2021).

The floor and roof diaphragms were connected to the vertical structural system by attaching the diaphragm joists to the flange of the wall studs via a combination of rim track and clip angle solution as a ledger framing system [e.g., Fig. 2(b)]. The diaphragm joists were oriented perpendicular to the longitudinal direction of the building (direction of shaking), resulting in a clear span length of ~2.9 m (9 ft 6 in.) for the room span and ~1.1 m (3 ft 6 in.) for the corridor span. Irrespective of the span length, the diaphragm framing was consistently constructed using 1000S200-54 at 610 mm (24 in.) o.c. for the joists (aligned with the vertical wall studs) and 1000T200-54 for the rim tracks at all floors of the building including the roof (Fig. 3). Both the diaphragms contained midspan blocking to enhance their shear capacity. The floor sheathing consisted of fiber-reinforced cement boards bonded with a layer of 0.838 mm (0.033 in.) thick (20 gauge) sheet steel. The thickness of cement boards was 14 mm (9/16 in.) at Floor 2 through Floor 6 and 11 mm (7/16 in.) at the roof.

The floor sheathing was attached to the upperside of the joists and rim tracks using #8 drywall screws at 152 mm (6 in.) o.c. both in the field and on the boundary. In addition, the underside of Floor 3 and roof was sheathed with 16 mm (5/8 in.) thick regular gypsum panels to provide a compartmentalized fire-testing environment. The gypsum panels were attached to the underside of the joists and rim tracks using #8 drywall screws at 152 mm (16 in.) o.c. both in the field and on the boundary. Additional information regarding the construction details of the structural systems has been given by Wang et al. (2016).

Building Construction

Construction of the test building commenced with the installation of the CFS base tracks (bottom tracks of the first level walls) as part of the building to shake-table tie-down plan. A total of 80 large-diameter post-tensioned rods were used to attach the base tracks

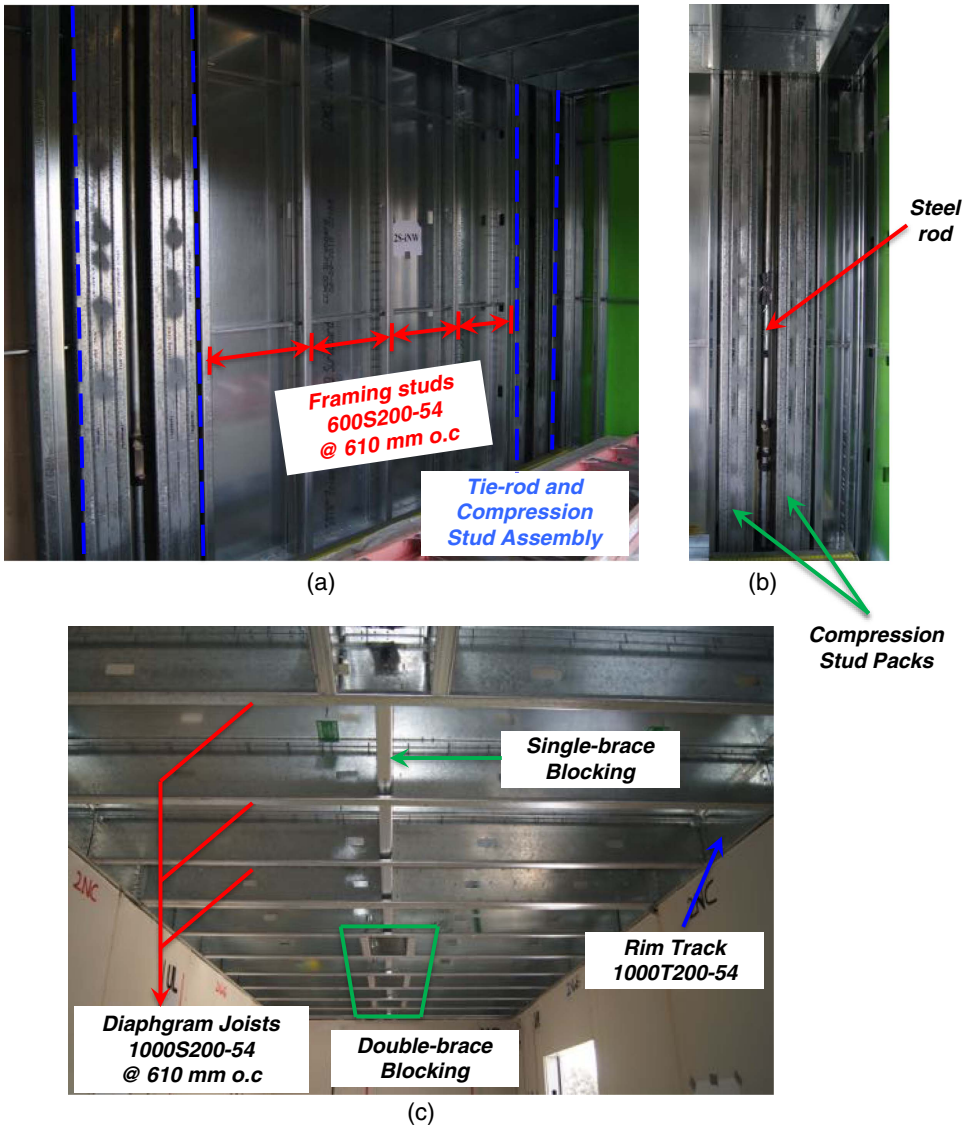

Fig. 2. Structural components framing details: (a) corridor shear wall; (b) tie-rod and compression stud assembly; and (c) floor diaphragm. (Images by Xiang Wang.)

to the table at a space at 0.6 m (2 ft) along the tracks. Subsequently, the first-level wall system was fabricated in situ during a period of approximately 4 days. Following the wall system installation at the first level, the construction process was significantly expedited by taking advantage of panelized construction. The prefabricated wall and floor panels were assembled onsite to form the structural skeleton of the remainder of the building at a rate of one story per day. As a result, the building structural skeleton was complete within 9 construction days. Interior construction commenced immediately following the completion of the building erection and spanned about an entire month. Activities related to interior construction included (1) installation of interior gypsum panels (structural walls, nonstructural walls, and ceiling), (2) installation of interior partition walls, and (3) other nonstructural components (e.g., doors and house appliances).

Instrumentation Plan

The building was outfitted with more than 250 analog sensors, a Global Positioning System (GPS) system, and an array of more than 40 digital video cameras to record the behavior of the structural components and building during the earthquake tests. In addition, remote-sensing systems, such as unmanned aerial vehicles (UAVs) and light ranging and detection (LiDAR) systems, were employed to collect imagery data to document the building conditions at various stages during the construction and test phases (Wang et al. 2020). Particularly, the seismic response of the test building was monitored with a dense array of analog sensors consisting of accelerometers, displacement transducers (string potentiometers and linear potentiometers), and strain gauges. They were connected to a multinode distributed data acquisition system and set to sample at a frequency of 240 Hz. Table 1 summarizes the four different types of analog sensors and the corresponding measured responses.

Because the present paper focuses on the system-level seismic behavior of the test building, experimental data of interest include the floor accelerations measured by the accelerometers as well as floor displacements measured by the string potentiometers at the lower four floors and the GPS at the roof of the building. Shear wall local responses measured by the string potentiometers and strain gauges are discussed in the companion paper (Wang and Hutchinson 2021).

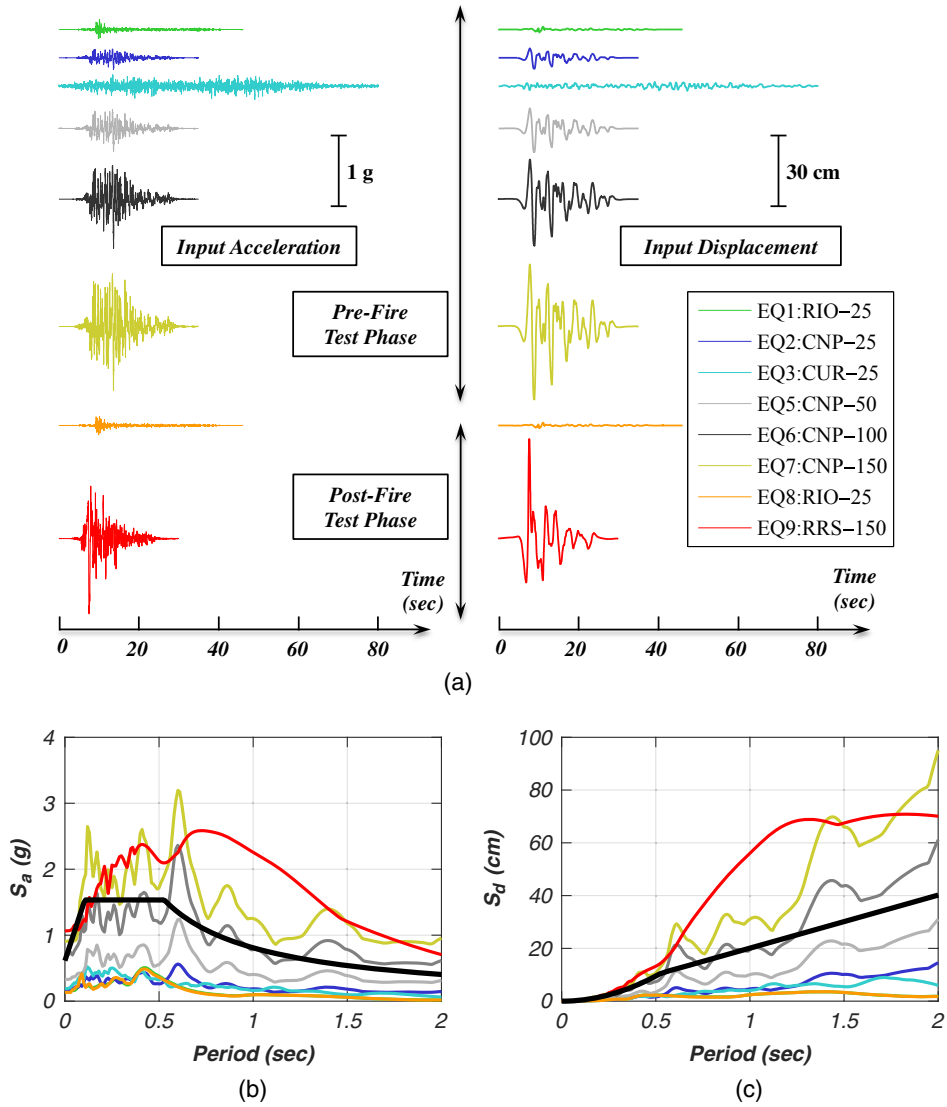

Fig. 3. Achieved earthquake input motions: (a) acceleration and displacement time histories; (b) 5% damped elastic pseudoacceleration spectra; and (c) 5% damped elastic displacement spectra (1 cm = 0.3937 in.). Thick solid lines as shown in the spectra plots indicate the ASCE 7 design spectra. (ASCE 2016.)

Table 1. Summary of analog sensors and their location for the seismic response monitoring

Sensor type	Type and locations of measurements
Accelerometer	Floor accelerations on all floors including the table platen
String potentiometer	Shear wall distortion at Levels 1, 2, and 4; floor displacements at lower four floors
Linear potentiometer	Shear wall uplift at Levels 1, 2, and 4; floor joist displacements at Floor 2
Strain gauge	Tension rod strains at Levels 1, 2, and 4, compression poststrains at Level 1

During the live fire tests, the test building was instrumented with ~230 thermocouples (Type K thermocouples with 24-gauge wires) to measure the temperature responses of the fire compartments and adjacent spaces. Importantly, thermocouple trees were installed at the center of each interior (room) compartment and the two ends of each corridor compartment to monitor the temperature profiles along the vertical direction [Fig. 4(b)]. All temperature data were recorded by a standalone data acquisition system with a sampling frequency of 1 Hz for a duration of approximately 1 h from the onset of fire ignition. Additionally, sacrificial video cameras were installed at various locations of the building interior to monitor smoke or fire spread. Detailed documentation of the instrumentation plans for all test phases is available from Wang et al. (2016).

Test Protocol

The 3-week test program consisted of a sequence of nine earthquake tests and six live fire tests in three test phases, namely: (1) prefire earthquake, (2) live fire, and (3) postfire earthquake (Table 2). During the prefire earthquake test phase, the building was subjected to seven earthquake tests using recorded ground motions scaled to increasing input motion intensity across a duration of 3 test days. Subsequently, live fire tests were conducted on the earthquake-damaged building at the second and sixth levels of the

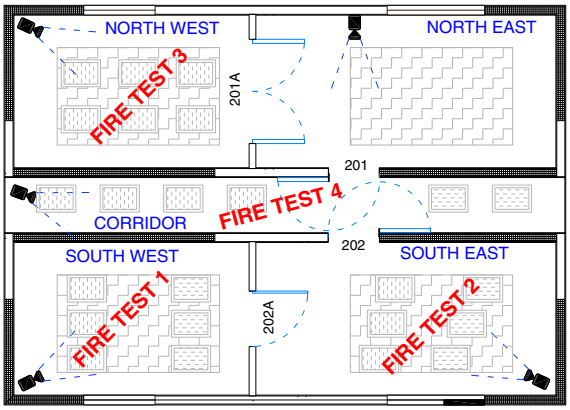

(a)

(b)

Fig. 4. Fire test protocol: (a) location of the fire compartments overlaid within the building plan layout; and (b) compartment fire test setup (southwest room at Level 2, Fire test 1) (image by Praveen Kamath).

Table 2. Summary of the test sequence and associated peak input motion and building responses

Test date	Test motion	Performance target	PIA (g)	$S_a(T_1, 5\%)$ (g)	PFA (g) (floor number)	PIDR (%) (level number)	PRDR (%)	RDR_{res} (%)
Day 1 (June 13, 2016)	EQ1:RIO-25	SLE	0.14	0.28	0.35 (R)	0.08 (L4)	0.05	0.0
	EQ2:CNP-25		0.17	0.32	0.38 (R)	0.09 (L4)	0.07	0.0
	EQ3:CUR-25		0.19	0.34	0.45 (R)	0.10 (L4)	0.08	0.0
Day 2 (June 15, 2016)	EQ4:CNP-25		0.17	0.35	0.43 (R)	0.10 (L4)	0.09	0.0
	EQ5:CNP-50	50% design	0.33	0.67	0.85 (R)	0.24 (L3)	0.19	0.0
	EQ6:CNP-100	Design	0.69	1.37	2.07 (R)	0.89 (L4)	0.70	0.0
Day 3 (June 17, 2016)	EQ7:CNP-150	MCE	0.91	2.01	3.77 (F5)	1.70 (L4)	1.49	0.1
			Fire test sequence (June 27–29, 2016)					
Day 4 (July 1, 2016)	EQ8:RIO-25	SLE	0.13	0.09	0.16 (R)	0.17 (L3)	0.12	0.0
	EQ9:RRS-150	MCE	1.07	2.54	4.43 (F5)	12.15 (L2)	2.84	1.2

Note: PIA = peak input acceleration; $S_a(T_1, 5\%) = 5\%$ damped elastic spectral acceleration of the input motion (T_1 represents the fundamental period of the building); PFA = peak floor acceleration; PIDR = peak interstory drift ratio; PRDR = peak roof drift ratio; RDR_{res} = residual roof drift ratio; SLE = service level earthquake; and MCE = maximum considered earthquake.

building across a duration of 3 consecutive days. The test program concluded with two postfire earthquake tests on the final test day. To complement the earthquake and fire test sequence, low-amplitude vibration tests in the form of white noise and ambient vibration tests were conducted throughout the construction and test phase. All earthquake and white-noise test motions were applied in the east–west direction using the single-axis shake table, whose axis coincided with the longitudinal axis of the building [Fig. 1(b)].

Earthquake Test Protocol

Earthquake motions were selected for the shake-table testing considering the following primary objectives: (1) inclusion of multiple intensity levels in the seismic test protocol, (2) design level event representative of strong earthquakes in California, and (3) inclusion of earthquake events with a wide variety of motion characteristics (e.g., near-fault pulse effect and strong durations). Guided by these selection criteria, three seed motions recorded during the shallow

earthquake events in California, namely CNP and RRS (both from the 1994 Mw = 6.7 Northridge earthquake), RIO (from the 1992 Mw = 7.0 Cape Mendocino earthquake), and CUR (from the 2010 Mw = 8.8 Maule subduction earthquake event in Chile), were selected as the input motions for the earthquake tests. The large-magnitude subduction record CUR contained significantly longer motion duration than the other three motions recorded during the Californian shallow earthquakes. Furthermore, record RRS differed fundamentally from the other three records because this near-fault earthquake motion is characterized by an appreciable velocity pulse and a wide spectral peak in the period range between 0.5 and 1 s (even larger than its short-period spectral accelerations). Additional information regarding the seed motion metadata (e.g., station, earthquake source, and fault mechanism) is available from Wang et al. (2016).

Scaling of the seed motions was undertaken to define a loading scenario that would impose gradually increased seismic performance levels to the test building, namely serviceability, design, and maximum considered. The acceleration and displacement time histories of the achieved input earthquake motions and the associated response spectra are shown in Fig. 3. The first seven earthquake motions (prefire test sequence) were applied at increasing intensity to progressively damage the building with the peak input accelerations of the motions increasing from $0.15g$ to $0.9g$ and the spectral accelerations at the fundamental period of the test building increased from $0.3g$ to $2.0g$ (Table 2). The last two test motions (postfire test sequence) were intended to represent a service-level aftershock event, EQ8 (a repeat of motion EQ1), and a near-fault extreme earthquake event, EQ9, with a peak input acceleration above $1.0g$. Test motion EQ9 was strategically selected to impose large seismic demands on the building that underwent significant period elongation (with a fundamental period of ~0.9 s prior to the test) due to the earthquake- and fire-induced damage accumulation.

Fire Test Protocol

Following the prefire earthquake test sequence, the earthquake-damaged building was subjected to live fire tests at six predetermined fire compartments, namely four tests at Level 2 and two tests at Level 6, on 3 consecutive test days. Fig. 4(a) illustrates the fire test sequence and the associated locations of the fire compartments overlaid within the building plan layout. The lower and upper floors (Levels 2 and 6) were selected to demonstrate the contrasting post-earthquake fire performance of the compartments with varied severity of earthquake damage. Although the upper floors were anticipated to be subjected to greater acceleration demands, the lower floors were envisioned to cumulate larger drift demands and thus sustain more severe damage, leading to more detrimental spread of temperature, flame, and smoke.

The compartments were all constructed with architectural features representative of a 60-min fire-resistance rating construction details (NFPA 2013). To ensure the attainment of a postflashover condition, the fire compartments were each filled with 12 L of n-heptane fuel in six stainless-steel burner pans to produce the anticipated fire loads, with an expected heat release rate of 2.16 MW [Fig. 4(b)]. The compartment ventilation characteristics and the severity of damage to the interior gypsum boards induced by prior earthquake tests were the major variables considered in these fire tests.

Building Dynamic Characteristics

Low-amplitude white-noise (WN) base excitation tests were consistently conducted before and after each earthquake test, with the exception of the final Test EQ9 due to the severity of building damage. This allowed investigation of the evolution of the dynamic characteristics (e.g., natural periods and damping ratios) of the test building at the various stages of the multihazard test program. Each WN test phase involved two individual tests with their base excitations scaled to distinct amplitudes measured in terms of the root-mean square (RMS) accelerations of the input excitations, namely, $1.5\%g$ RMS or $3.0\%g$ RMS. The modal parameters of the building are extracted using the deterministic-stochastic identification method, namely a time-domain system identification technique, that realizes a linear state-space model using input-output acceleration data (Van Overschee and De Moor 1996). Further details regarding the implementation of system identification analysis procedures have been given by Wang and Hutchinson (2020). These dynamic parameters are essential for understanding the seismic behavior of the test building and in particular correlating the dynamic properties with the structural damage during the multihazard test program.

Fig. 5 illustrates the evolution of the natural periods and damping ratios associated with the building fundamental mode in the direction of shaking. Damage states S1–S9 shown in the figure correspond to the individual states of the building throughout the test program (from service, design, MCE, fire, to postfire earthquake tests). During the prefire earthquake test phase (EQ1–EQ7), the fundamental period of the building elongated as a result of the increased earthquake intensity and larger seismic demands. As indicated by the $3.0\%g$ RMS WN test results, the initial fundamental

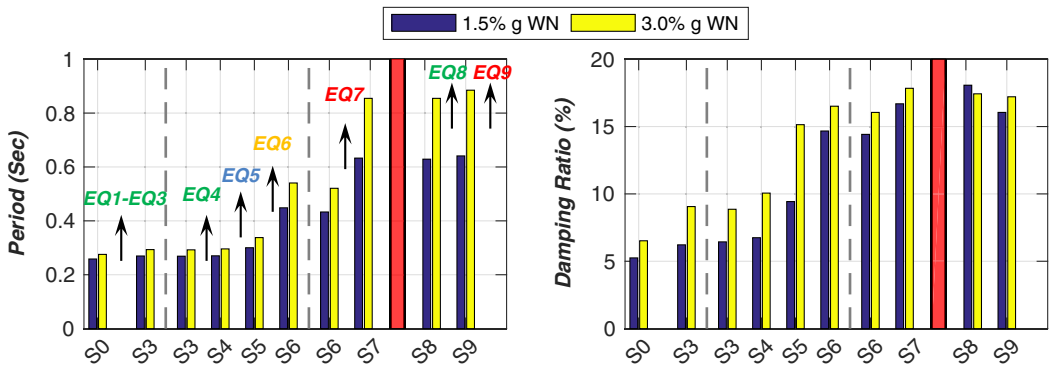

Fig. 5. Evolution of the natural periods and damping ratios associated with the building fundamental mode. Dashed line divides earthquake test dates, and red bar denotes the fire test phase.

J. Struct. Eng., 2021, 147(9): 04021125

period of ~0.25 s during the service-level test sequence (EQ1–EQ4) nearly doubled (>0.5 s) following the design test (EQ6) and increased by more than threefold (~0.9 s) following the MCE test (EQ7).

Correspondingly, the damping ratio associated with the fundamental mode increased from <10% during the service-level test sequence to >15% following the design event as a result of accumulated structural damage with the increased earthquake intensity. Notably, the modal parameters of the building underwent no substantial variations following the fire tests, which implies that earthquake-induced damage accumulated during the prefire test phase significantly outweighed the effect of fire-induced damage to the building. Furthermore, the natural periods and damping ratios appear to be dependent on the WN excitation amplitudes, particularly when the building damage became more pervasive following the design event EQ6 (S6 and the ensuing states). Increasing the amplitude from 1.5%g RMS to 3.0%g RMS led to a 10%–20% increase of the natural periods and a 20%–30% rise of the damping ratios.

Building Responses and Physical Damage

This section presents the system-level building responses (e.g., floor accelerations, interstory drifts, residual displacements, and story shear forces) during the prefire and postfire earthquake test phases as well as the observed seismic damage of the test building during each test phase. Furthermore, the compartment temperature responses during the live fire tests and the observed fire damage to the building are summarized to characterize the impacts of compartment fire hazards on the building structural system. Importantly, the physical condition of the building was inspected at different stages throughout the experimental program, namely (1) pretest, (2) post-service-level earthquake (SLE) (following Test EQ3), (3) post-design earthquake (DE) (following Test EQ6), (4) post-MCE (following Test EQ7), (5) following the fire test phase, and (6) end of test program (following Test EQ9). In addition, rapid inspections were conducted between the tests during the test days that involved multiple earthquake tests, although the primary purpose of these inspections was to examine the condition of critical structural components (e.g., mass plate anchorage and tie rod coupler connections).

Summary of Building Peak Responses

To facilitate discussion of the test building performance during the prefire and postfire earthquake tests, the earthquake input motion and system-level building responses in the direction of shaking (along the longitudinal axis of the building) are summarized in Table 2. These comparisons immediately articulate that all building seismic demands increased during the imposition of the sequential earthquake motions during the prefire earthquake test phase. In what follows, a floor-by-floor assessment is performed to guide the interpretation of the distribution of these seismic demands during each earthquake test. Because direct displacement measurements were available only at select floors (the lower four floors and roof), the interstory drift is determined by taking the differential displacement of the two adjacent floors via double integrating the accelerations of the corresponding floors, whereas direct displacements at the roof and the shake-table platen are employed to determine the roof drift response and the residual drifts.

Prefire Earthquake Tests

Building Responses

Although relatively small in amplitude during the service level earthquakes [peak interstory drift ratio (PIDR) <0.1%], the PIDRs achieved about 1% during the design event (EQ6) and exceeded 1.5% during the MCE event (EQ7). Fig. 6 shows the story shear versus interstory drift ratio (IDR) response of Level 4, where the drift demand attained the largest value among all levels during the prefire earthquake test phase. These hysteretic responses demonstrate that the test building remained quasi-linear during the service-level test (EQ2) as a result of small drift demands but became highly nonlinear as the drift demands reached ~0.8% during the design event (EQ6) and exceeded 1.5% during the MCE event (EQ7). The story-level hysteretic characteristics of the shear walls observed from the building tests correlate well with the pseudo-static cyclic test results of the shear wall components, which were constructed using similar framing details and dimensions to emulate the corridor shear walls of the test building (Hoehler et al. 2017).

Fig. 7 presents the normalized peak base shear versus peak roof drift ratio (PRDR) response during the prefire test sequence. These plots demonstrate that the building responded almost elastically up to the 50% design event (EQ5). This observation is consistent with physical observations, discussed subsequently, where only minor damage was noted. Although the base shear increased in proportion with the motion intensity for the design event (EQ6), the roof drift ratio increased threefold between the 50% design event (EQ5) and the design event (EQ6). This is indicative of the onset of nonlinear deformation of the test building. With a further increase of the motion intensity by 50% during the MCE event (EQ7), the roof drift continued to increase and doubled the demand achieved during the design event (EQ6), whereas the base shear demand remained

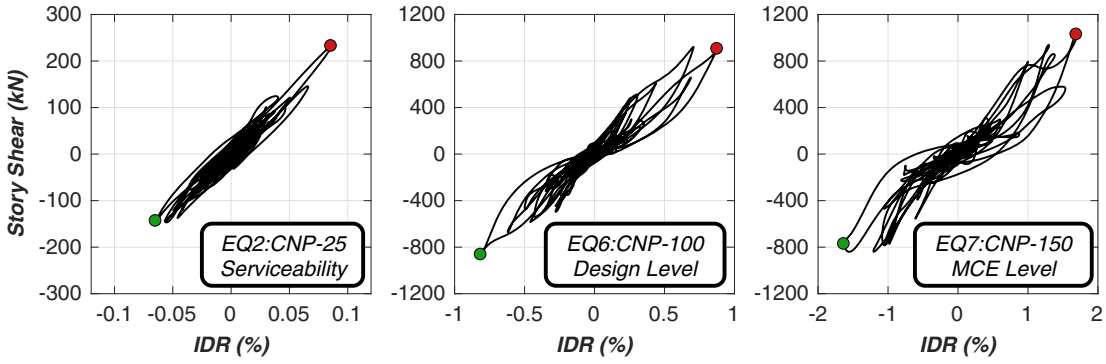

Fig. 6. Story shear versus interstory drift ratio at Level 4 during three prefire earthquake tests (1 kN = 0.2248 kips).

J. Struct. Eng., 2021, 147(9): 04021125

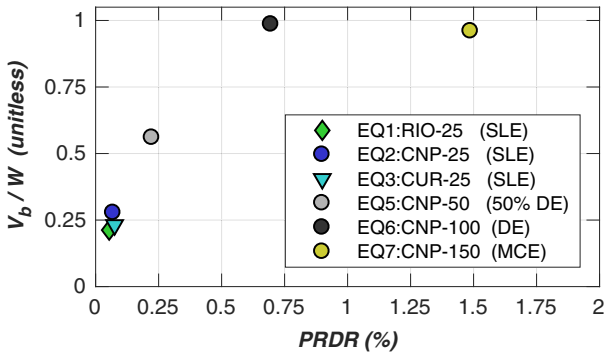

Fig. 7. Peak normalized base shear forces versus peak roof drift ratio.

comparable to that of the design event (EQ6). This observation demonstrates that the lateral system of the test structure attained its peak strength following the design event (EQ6).

Physical Damage

Due to the low seismic demands during the service-level tests at all levels of the test building [peak floor acceleration (PFA) <0.5*g* and PIDR < 0.1%], the interior sheathing sustained only a few instances of minor damage in the form of incipient screw withdrawal and localized gypsum crushing and bulging at corners and adjacent panel locations. This type of damage was detected only at Levels 3 and 4, and no visible damage to interior gypsum sheathing occurred at other levels. The extent of gypsum sheathing damage, however, was considered minimal. Damage to the interior sheathing continued to develop as the seismic drift demand increased during the design (EQ6) and MCE (EQ7) events. Screw withdrawal and gypsum crushing of the corridor shear walls and gravity walls became more pervasive at all but the uppermost levels, in particular at the corridor shear wall–gravity wall boundaries as well as the window and door openings (Fig. 8).

In contrast, damage to the exterior shear walls sheathing remained restricted because they occurred only in the form of localized gypsum crushing at the corner and formation of gaps between

Fig. 8. Gypsum sheathing damage of the Level 4 corridor shear wall and gravity wall at the end of the prefire earthquake test phase. SW = shear wall, and GW = gravity wall, and dashed line indicates the boundary between shear wall and gravity wall. (Images by Xiang Wang.)

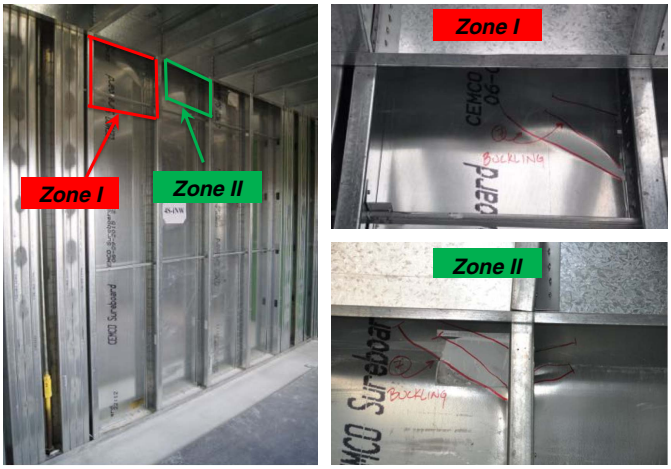

Fig. 9. Structural sheathing sheet steel local buckling of the Level 4 corridor shear wall at the end of the prefire earthquake test phase. (Images by Xiang Wang.)

gypsum panels. Following the completion of the prefire earthquake test sequence, the room-side gypsum panels of the northwest compartment at Level 4, the level with the largest drift demands during the prefire test sequence, were removed to allow for inspection of the shear wall framing and sheathing steel of the corridor-side structural panels (Fig. 9).

This inspection revealed that localized buckling of the sheathing steel occurred at the top of the shear wall, whereas its framing studs and tracks did not sustain apparent damage. In addition, very loose tie rods were observed at the end of the prefire test sequence. However, attributing the occurrence of tie-rod loosening to a specific earthquake test was not feasible because the tie rods were not accessible until removal of the gypsum sheathing, which occurred at the end of the prefire earthquake test sequence. In contrast, the exterior shear wall in the same compartment sustained no apparent damage to the wall framing and sheathing steel, nor the occurrence of loosened tie rods. Because the tie rods provide the essential uplift resistance in CFS lateral systems, further investigations are recommended to assess the system-level uplift-resisting behavior of the CFS structures due to the occurrence of tie-rod loosening as well as its impact on the overall structural response.

Fire Tests

Following the prefire earthquake tests, live fire tests were conducted at the six predetermined compartments at Levels 2 and 6. Fig. 10 presents the compartment temperature responses during all six fire tests, which were measured by the thermocouple trees located at the approximate center of each interior (room) compartment and the two ends of each corridor compartment (Fig. 4). The thermocouple trees each consisted of six vertically distributed thermocouples, whose distances from the compartment ceiling ranged from 0.1, 0.5, 0.8, 1.1, and 1.4 m to 1.8 m (indicated in figure legends). However, sensor errors of select thermocouples occurred due to the loss of protection against elevated temperature, and therefore data recorded by the malfunctioned sensors are excluded from the results.

The temperature responses of all interior (room) compartments are characterized by a double-peak pattern, as shown in Figs. 10(a and b). The compartment temperatures increased rapidly and reached the first peaks of 700°C–800°C in ~60 s from the onset of fire ignition, indicating the attainment of the flashover conditions

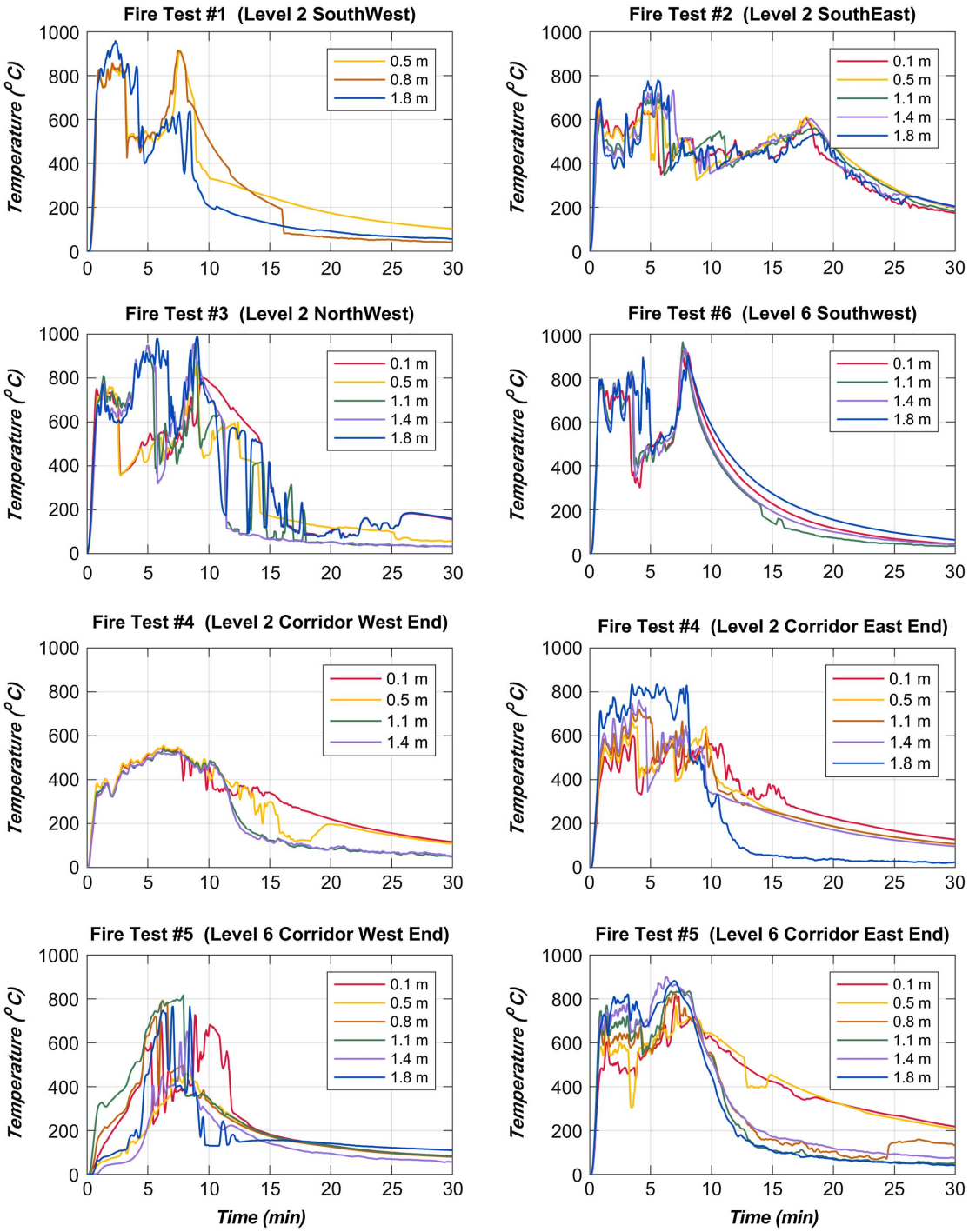

Fig. 10. Fire compartment temperature responses during the live fire tests. Value shown in the legend represents the distance of the thermocouple as measured from compartment ceiling.

in all fire test compartments. Dependent on the atmospheric effect on the compartment fire dynamics following the flashover, the temperatures attained the second peaks of 800°C–1,000°C in 300–450 s and subsequently descended to ~400°C, which was indicative of fuel burnout.

Comparison of the fire test results reveals that the temperature behavior of the southeast compartment at Level 2 (Fire test 2) differed from the remaining three compartments, as evident by slightly lower peak temperatures (~800°C) but longer duration prior to the temperature drop (>18 min). This is primarily attributed to the differences in the compartment ventilation conditions because the window opening at the southeast compartment at Level 2 was partially enclosed by fire rated gypsum boards during the test, whereas the window openings of the other three interior compartments remained fully unenclosed. In contrast to the interior compartments, the temperature responses of the corridor compartments appeared more susceptible to the atmospheric conditions due to the configuration of the openings and their orientation relative to the prevailing wind direction. The prevailing wind direction was eastward during both corridor live fire tests.

Consequently, the temperature behavior of the corridor compartments, shown in the lower Figs. 10(c and d), differed from those

of interior compartments in the following two major aspects: (1) the temperature responses were characterized by a single plateau instead of two peaks until the fuel burnout, and (2) the temperatures of the downwind (east) end of the corridor were consistently larger than those of the upwind (west) end. Regardless, the peak temperatures attained in the corridor compartments at the downwind end were comparable with those of the interior compartments (~800°C).

The elevated compartment temperatures during the fire tests resulted in dehydration and shrinkage of the wall and ceiling gypsum boards and fiber cement boards on the floor diaphragms [Figs. 11(b and c)]. Fire-induced damage to the wall and floor sheathing resulted in significant strength and rigidity loss of these structural components. Specifically, the fire-induced structural damage occurred in the form of (1) partial detachment of gypsum ceilings [Fig. 11(b)], and (2) significant deflections (~1.5 cm) of the floor diaphragm at the second floor as a result of deteriorated cement boards on top of the sheet steel [Fig. 11(d)]. In addition, the building egress was compromised following the fire tests as a result of the loss of functionality of the doors due to the fire-induced damage to the door components [Fig. 11(e)].

Postfire Earthquake Tests

The postfire earthquake test sequence involved a service-level aftershock event (EQ8: RIO-25, which was a repeat of test motion EQ1: RIO-25) and a near-fault extreme event (EQ9: RRS-150). Due to the low seismic demands (PIDR < 0.2% and PFA < 0.2g), the service level aftershock test (EQ8) introduced no additional damage to the test building. In contrast, the final near-fault extreme event (EQ9) induced excessively large drift demands at Level 2 of the test building (PIDR > 12% and residual drift of ~6%) and consequently resulted in extremely severe damage to the structural system at this level. In this regard, an important aspect of the subsequent discussion within this section involves presenting the building displacement responses during this final earthquake test (EQ9) and the ensuring structural damage. Moreover, the postfire earthquake test results are compared with those of the prefire counterparts in an effort to contrast the response characteristics of the building with different damage conditions.

Building Displacement Responses and Physical Damage

Fig. 12 presents the interstory drifts at the lower three levels and the building residual drift profile associated with the final extreme event test (EQ9). These responses are derived using the direct floor displacement measurements recorded by the string potentiometers at the lower four floors and the GPS at the roof level. The interstory drift results reveal that Level 2 of the building sustained excessive drift demands with a PIDR > 12% and a residual drift ratio of ~6%, which were substantially larger than the corresponding demands of the adjacent levels [Fig. 12(a)]. Additionally, the building residual drift profile clearly indicates the formation of a soft-story mechanism at Level 2 of the building at the completion of the test program [Figs. 12(b and c)] because the residual story drift of Level 2 (~19 cm) accounted for ~85% of the total residual drift of the building (~22 cm at the roof).

The final building inspection (post-EQ9) involved detailed documentation of the damage of the gypsum sheathing and subsequently the steel framing and the sheathing steel of the structural panels by removing the room-side interior gypsum panels. Importantly, the severe damage to the structural components of Level 2 revealed the ultimate damage mechanism of the building lateral-loading resisting system. Evident in the final inspection was the near-complete tearing of a large extent of the structural sheathing, partial or full delamination of sheathing face gypsum, and associated detachment of the gypsum on the opposite side of the shear walls (Fig. 13).

Consequently, the structural integrity of the shear walls was compromised due to extensive global and local buckling of the wall framing members [Figs. 13(b and c)]. The test building, however, resisted collapse largely due to redistribution of loads and the framing action provided by the continuous tie-rod and compression stud

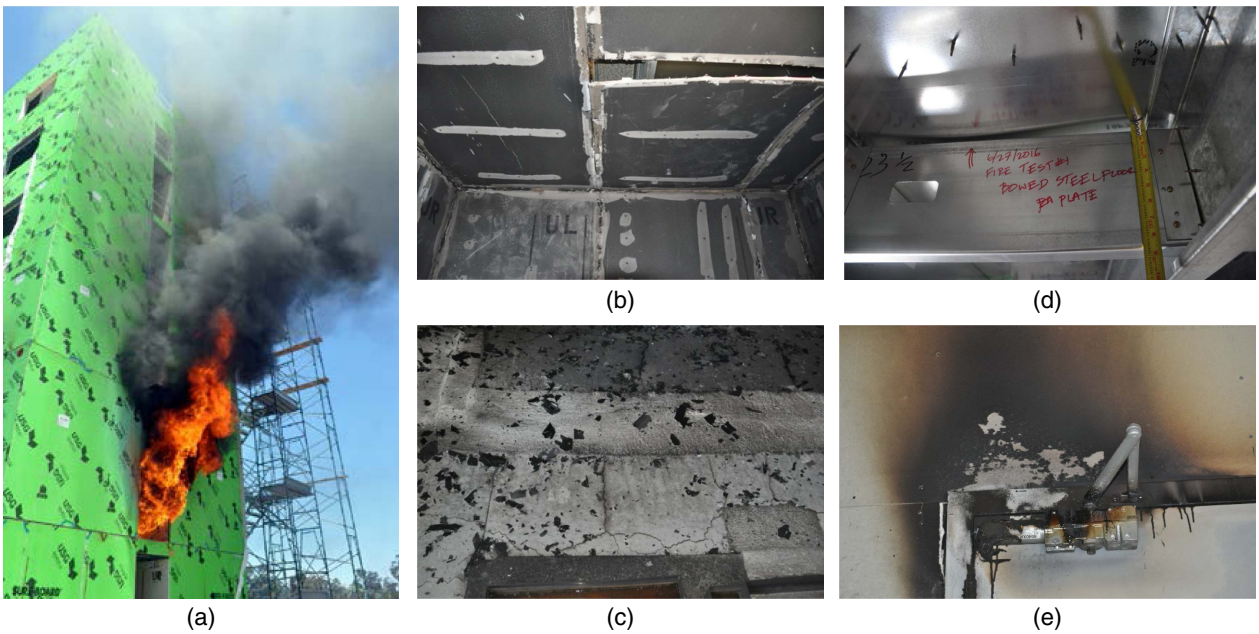

Fig. 11. Fire-induced damage to the building system: (a) flame and smoke extension through the east corridor opening (Fire test 3); (b) partially detached ceiling gypsum board; (c) shrinkage and cracking of the cement board on the floor; (d) excessive floor deflection due to diaphragm sagging; and (e) melted door closer latch. (Images by Xiang Wang.)

J. Struct. Eng., 2021, 147(9): 04021125

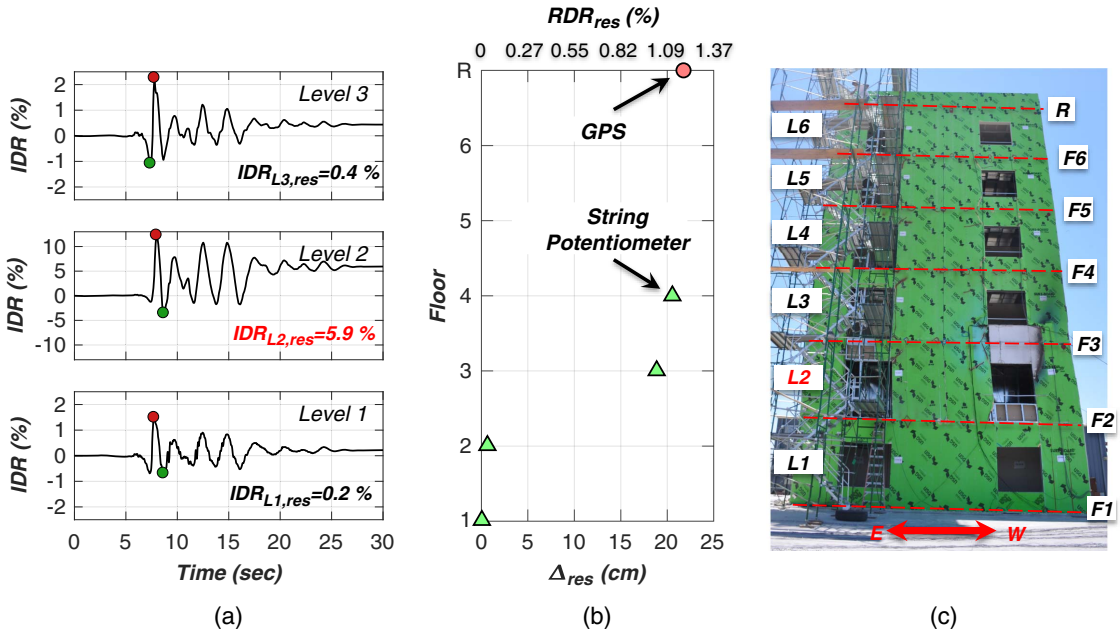

Fig. 12. Building responses associated with the final extreme event test (EQ9): (a) interstory drift ratio responses of the lower three levels; (b) building residual drift profile at the end of the test program (1 cm = 0.3937 in.); and (c) north elevation of the building at the end of the test program. Arrow denotes the direction of shaking, L# denotes level number, and F# denotes floor number. (Images by Xiang Wang.)

Fig. 13. Interior view of the Level 2 corridor shear wall damage at the end of the test program (arrow denotes the direction of shaking): (a) corridor (viewing eastward); (b) southwest room; (c) buckling and bending of framing stud precipitated by loss of sheathing fasteners; and (d) structural panel fastener tearing. (Images by Xiang Wang.)

system. Although all remaining levels of the building achieved moderately larger drift demands during the postfire extreme event test (EQ9) compared with those attained during the prefire test phase, structural damage at these levels was restricted to the wall sheathing damage, whereas the shear wall framing members remained uncompromised at the final inspection stage.

Prefire and Postfire Building Response Comparison

Peak Floor Accelerations and Interstory Drift Demands

Fig. 14 compares the building PFA and PIDR responses during the service-level events prefire and postfire (i.e., Tests EQ1–EQ3 and EQ8). The distributions of the peak responses demonstrate that the acceleration demands of the building were markedly attenuated, whereas the drift demands almost doubled during the postfire service-level Test EQ8 in comparison with those achieved during the prefire service-level tests (EQ1–EQ3). This is due to the fact that the building sustained substantial stiffness deterioration and period elongation due to the structural damage accumulated during the prior earthquake and fire tests.

In contrast, Fig. 15 presents the building PFA and PIDR responses during the above-service-level events (i.e., Tests EQ5–EQ7 and EQ9). These results reveal that as the motion intensity increased, the largest PIDR reached ~1.0% during the design motion Test EQ6 and above 1.5% during the MCE motion Test EQ7.

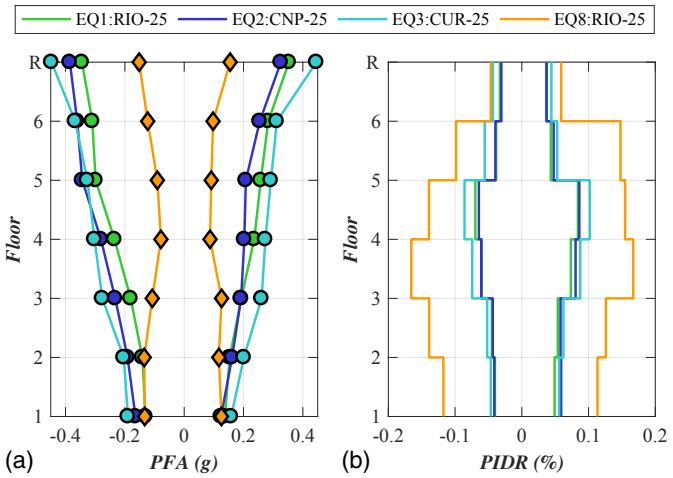

Fig. 14. Building peak responses during the service-level tests: (a) peak floor accelerations; and (b) peak interstory drift ratios.

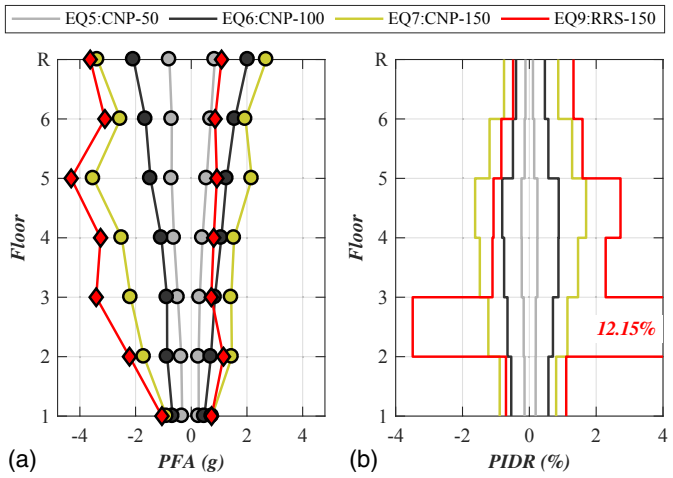

Fig. 15. Building peak responses during the above-service-level tests: (a) peak floor accelerations; and (b) peak interstory drift ratios.

The largest PIDR occurred at the building midheight (i.e., Level 4) throughout the prefire earthquake test sequence. The vertical distribution of the PIDRs is consistent with building physical observations. In addition, the PFA increased almost monotonically up the height of the building during the prefire earthquake test sequence, indicating a fundamental-mode dominant structural response in these tests.

In contrast, the final earthquake test (near-fault extreme event EQ9) subjected the building to excessively large drift demands particularly at Level 2, which sustained a peak interstory drift ratio of above 12%. The extreme drift demands achieved during this test resulted in a near-collapse condition of the specimen, with its lateral resistance almost solely provided by the tie-rod and compression stud system, as discussed subsequently. The residual roof drift ratio of the building exceeded 1% following Test EQ9 (Table 2). This may be partially attributed to the fire-induced damage to the gypsum sheathing at Level 2, which reduced the shear capacity of the shear walls and consequently led to the formation of a soft-story mechanism during the final near-fault earthquake (EQ9) at this level.

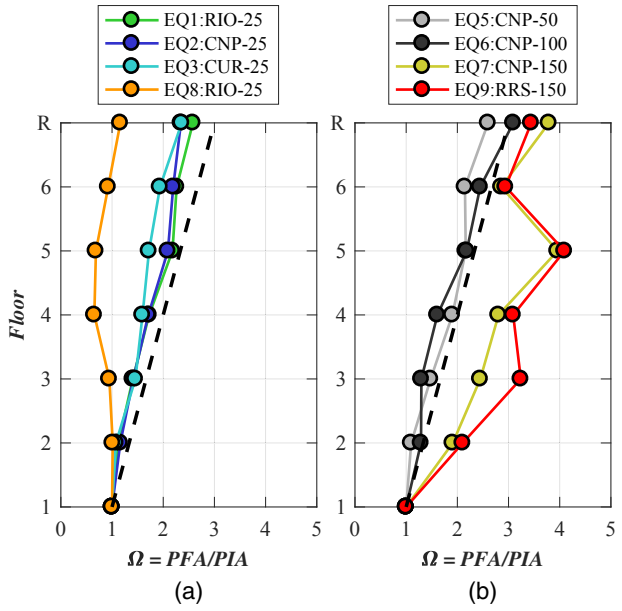

Fig. 16. Acceleration amplification ratios of the test building under (a) service-level tests; and (b) above-service-level tests. PFA = peak floor acceleration, PIA = peak input acceleration, and dashed line represents the empirical equation $1 + 2z/h$ per ASCE 7 provisions (ASCE 2016).

Floor Acceleration Amplification

Fig. 16 compares the acceleration amplification ratio Ω of the test building during the earthquake tests. The acceleration amplification ratio Ω is determined as the ratio of the peak acceleration achieved at each floor to the peak acceleration of the input motion. Per ASCE 7 code provisions (ASCE 2016), the floor amplification ratio is empirically considered using the linear equation $1 + 2z/h$ (where z/h denotes the normalized building height). Specifically, this linear distribution indicates an amplification ratio of 1.0 at the base to 3.0 at the roof of the building (thick dashed lines in Fig. 16). During the prefire service-level test sequence (EQ1–EQ3) [Fig. 16(a)], the acceleration amplification ratio increased monotonically up the height of the building with the largest values ranging between 2.0 and 2.5 at the roof, which is slightly lower than the code-specified value of 3.0.

Acceleration amplification continued to increase during Tests EQ5 and EQ6 as the motion intensity increased [Fig. 16(b)]. The amplification distribution achieved during the design event (Test EQ6) agrees well with the code-specified distribution along the building height. In contrast, as the building sustained significant period elongation following the prior earthquake and live fire tests, the postfire service-level Test EQ8 resulted in a significantly attenuated acceleration distribution over the building height (with $\Omega \sim 1.0$ at the roof level). During the two MCE events, namely Tests EQ7 and EQ9, the floor acceleration amplification ratios were significantly larger than the code-specified distribution at all floors [Fig. 13(b)]. Additionally, the largest acceleration amplification during these MCE events occurred in the middle of the building (Level 5) instead of the roof.

Conclusions

A substantial growth in the use of CFS framed construction has recently been observed, notably in high seismic regions in the

western US. Structural systems of this kind consist of light-gauge framing members (e.g., studs, tracks, and joists) attached with sheathing materials (e.g., wood and sheet steel). CFS structures, owing to several beneficial attributes such as high strength-to-weight ratio and noncombustibility, lend themselves to resilience against both earthquake and fire hazard scenarios. Although these light-framed systems provide the potential to support the need for resilient and sustainable housing, the state of understanding regarding their structural behavior in response to extreme events, in particular earthquakes and ensuing hazards, remains relatively limited.

With the objective of advancing knowledge regarding the multihazard performance of midrise CFS construction, a full-scale 6-story cold-formed steel building was constructed and tested on the UCSD Large High-Performance Outdoor Shake Table test facility. Within this 3-week test program, the test building was first subjected to a suite of seven earthquake motions with progressively increasing motion intensity, from service to MCE level. Following the first seven earthquake tests, live fire tests were conducted on the earthquake-damaged building in six strategically selected rooms to evaluate the performance of fire protection systems and the impact of seismic damage of the building and the associated characteristics of the fires that ensued. Finally, for the first time, the test building was subjected to two postfire earthquake tests, including a low-amplitude aftershock and an extreme near-fault target MCE-scaled motion.

In this paper, the test program is documented and test results specific to the global building responses and associated physical observations discussed, whereas the component-level behavior of the CFS shear walls and associated seismic design implications are discussed in a companion paper (Wang and Hutchinson 2021). Key findings associated with the three test phases described herein are summarized as follows:

- Prefire earthquake tests: The building suffered minimal damage during the service level earthquake tests and its response remained largely in the quasi-linear range, with very low drift demands applied to lateral load resisting system (interstory drift < 0.2%). During the design level earthquake test, the corridor shear and gravity walls at Levels 3 and 4 suffered damage in the form of gypsum panel crushing and fastener withdrawal when the interstory drifts at these two levels reached about 1.0%. This is corroborated by the fact that the building fundamental period increased by more than 50%. Damage continued to progress as the interstory drift exceeded 1.5% during the MCE test; however, observed damage to the building remained readily repairable, with the structural shear walls at the lower floors (those that could be inspected) developing their intended local steel sheathing buckling mechanism near attachment points along framing member perimeters. The building structural components performed satisfactorily throughout the prefire earthquake test sequence. The most significant damage to the structural system, as noted, occurred in the form of local buckling of the sheet steel on the corridor shear wall sheathing, an anticipated and desirable damage mechanism.
- Fire tests: Postflashover conditions were achieved in all six compartment fire tests at the given ventilation conditions, with the corresponding maximum compartment temperatures ranging between 800°C and 1,000°C. The elevated temperatures of the fire compartments caused significant degradation of the wall sheathing, namely the fire-rated architectural gypsum boards at the building interior and the face gypsum of the structural panels (sheet steel bonded with fire-rated face gypsum boards) on the corridor. Loss of stiffness of the floor sheathing was also noted due to degradation of the fiber-reinforced cement boards overlaid on the sheet steel, which may have preempted the development of significant floor deflections (~1.5 cm). Thermal bowing of floor sheathing as observed following the fire tests was indicative of the presence of high-temperature regions within the floor diaphragms during the fire tests. Dehydrated and partially detached ceiling panels were noted in several locations, which may cause potential overhead hazards in the case of an aftershock event as well as the increased likelihood of flame spread throughout the building and traveling fire hazards.
- Postfire earthquake tests: A low-amplitude service-level aftershock test imposed following the fire tests significantly attenuated seismic demands in the building as a result of the elongated period caused by the prefire earthquake sequence. In contrast, the extreme near-fault earthquake test (EQ9) resulted in development of a full soft-story mechanism at Level 2 and caused severe damage to the buildings structural system manifest in complete loss of structural integrity of the corridor and exterior shear walls along the longitudinal axis of the building. The test building, however, resisted collapse due to redistribution of loads to the building tie-down rod and compression pack system, which offered lateral resistance via frame-type actions.

Data Availability Statement

Some or all data, models, or code that support the findings of this study are available from the corresponding author upon request.

Acknowledgments

This research project is a collaboration between two academic institutions (University of California, San Diego, and Worcester Polytechnic Institute), two government or institutional granting agencies (Department of Housing and Urban Development and the California Seismic Safety Commission) and more than 15 industry partners. The authors also thank the Jacobs School of Engineering and Department of Structural Engineering at UCSD for matching support of this effort. Industry sponsors include the California Expanded Metal Products Co. (CEMCO) and Sure-Board, who each provided financial, construction, and materials support. Specific individuals that dedicated significant time on behalf of this effort include Fernando Sesma (CEMCO), Kelly Holcomb, Carleton Elliot, and Tyler Elliot (Sure-Board), Harry Jones (DCI Engineers), Diego Rivera (SWS Panels), Doug Antuma (Rivante), Larry Stevig (State Farm Insurance), Tim Reinhold and Warner Chang (Insurance Institute for Business and Home Safety), Steve Helland (DPR Construction), Rick Calhoun (Walters & Wolf), and Jesse Karnes (MiTek). The authors appreciate the efforts of these individuals and their colleagues at their respective firms. Regarding support for the test program, the efforts of NHERI@UCSD staff, namely, Robert Beckley, Jeremy Fitcher, Dan Radulescu, and Alex Sherman, and UCSD graduate student Srikar Gunisetty are greatly appreciated. Findings and conclusions presented herein are those of the authors and do not reflect the opinions of the sponsoring agencies or industry partners.

References

AISI (American Iron and Steel Institute). 2015a. *North American specification for the design of cold-formed steel structural framing*. AISI S240. Washington, DC: AISI.

AISI (American Iron and Steel Institute). 2015b. *North American standard for seismic design of cold-formed steel structural systems*. AISI S400. Washington, DC: AISI.

Al-Kharat, M., and C. A. Rogers. 2007. "Inelastic performance of cold-formed steel strap braced walls." *J. Constr. Steel Res.* 63 (4): 460–474. https://doi.org/10.1016/j.jcsr.2006.06.040.

ASCE. 2016. *Minimum design loads for buildings and other structures*. ASCE 7. Reston, VA: ASCE.

Balh, N., J. DaBreo, C. Ong-Tone, K. El-Saloussy, C. Yu, and C. A. Rogers. 2014. "Design of steel sheathed cold-formed steel framed shear walls." *Thin-Walled Struct.* 75 (Feb): 76–86. https://doi.org/10.1016/j.tws.2013.10.023.

Branston, A., Y. C. Chen, F. A. Boudreault, and C. A. Rogers. 2006. "Testing of light-gauge steel-frame—Wood structural panel shear walls." *Can. J. Civ. Eng.* 33 (5): 561–572. https://doi.org/10.1139/l06-014.

Fiorino, L., B. Bucciero, and R. Landolfo. 2019. "Shake table tests of three storey cold-formed steel structures with strap-braced walls." *Bull. Earthquake Eng.* 17 (7): 4217–4245. https://doi.org/10.1007/s10518-019-00642-z.

Fiorino, L., V. Macillo, and R. Landolfo. 2017. "Shake table tests of a full-scale two-story sheathing-braced cold-formed steel building." *Eng. Struct.* 151 (Nov): 633–647. https://doi.org/10.1016/j.engstruct.2017.08.056.

Fülöp, L., and D. Dubina. 2004. "Performance of wall-stud cold-formed shear panels under monotonic and cyclic loading: Part I: Experimental research." *Thin-Walled Struct.* 42 (2): 321–338. https://doi.org/10.1016/S0263-8231(03)00063-6.

Hoehler, M. S., C. M. Smith, T. C. Hutchinson, X. Wang, B. J. Meacham, and P. Kamath. 2017. "Behavior of steel-sheathed shear walls subjected to seismic and fire loads." *Fire Saf. J.* 91 (Jul): 524–531. https://doi.org/10.1016/j.firesaf.2017.03.021.

Iuorio, O., V. Macillo, M. T. Terracciano, T. Pali, L. Fiorino, and R. Landolfo. 2014. "Seismic response of CFS strap-braced stud walls: Experimental investigation." *Thin-Walled Struct.* 85 (Dec): 466–480. https://doi.org/10.1016/j.tws.2014.09.008.

Landolfo, R., L. Fiorino, and G. Della Corte. 2006. "Seismic behavior of sheathed cold-formed structures: Physical tests." *J. Struct. Eng.* 132 (4): 570–581. https://doi.org/10.1061/(ASCE)0733-9445(2006)132:4(570).

Liu, P., K. D. Peterman, and B. W. Schafer. 2014. "Impact of construction details on OSB-sheathed cold-formed steel framed shear walls." *J. Constr. Steel Res.* 101 (Oct): 114–123. https://doi.org/10.1016/j.jcsr.2014.05.003.

Macillo, V., L. Fiorino, and R. Landolfo. 2017. "Seismic response of CFS shear walls sheathed with nailed gypsum panels: Experimental tests." *Thin-Walled Struct.* 120 (Nov): 161–171. https://doi.org/10.1016/j.tws.2017.08.022.

NFPA (National Fire Protection Association). 2013. *Standard for fire doors and other opening protectives*. NFPA 80. Quincy, MA: NFPA.

NIST. 2016. *Seismic design of cold-formed steel lateral load-resisting systems: A guide for practicing engineers*. NIST GCR 16-917-38. Gaithersburg, MD: NIST.

Peterman, K. D., M. J. Stehman, R. L. Madsen, S. G. Buonopane, N. Nakata, and B. W. Schafer. 2016a. "Experimental seismic response of a full-scale cold-formed steel-framed building. I: System-level response." *J. Struct. Eng.* 142 (12): 04016127. https://doi.org/10.1061/(ASCE)ST.1943-541X.0001577.

Peterman, K. D., M. J. Stehman, R. L. Madsen, S. G. Buonopane, N. Nakata, and B. W. Schafer. 2016b. "Experimental seismic response of a full-scale cold-formed steel-framed building. II: Subsystem-level response." *J. Struct. Eng.* 142 (12): 04016128. https://doi.org/10.1061/(ASCE)ST.1943-541X.0001578.

Serrette, R., J. Encalada, M. Juadines, and H. Nguyen. 1997. "Static racking behavior of plywood, OSB, gypsum, and fiberboard walls with metal framing." *J. Struct. Eng.* 123 (8): 1079–1086. https://doi.org/10.1061/(ASCE)0733-9445(1997)123:8(1079).

Shamim, I., J. Dabreo, and C. A. Rogers. 2013. "Dynamic testing of single- and double-story steel-sheathed cold-formed steel-framed shear walls." *ASCE J. Struct. Eng.* 139 (5): 807–817. https://doi.org/10.1061/(ASCE)ST.1943-541X.0000594.

Van Overschee, P., and B. De Moor. 1996. *Subspace identification for linear systems: Theory, implementation, applications*. Boston: Kluwer.

Wang, X., and T. C. Hutchinson. 2020. "Evolution of modal characteristics of a mid-rise cold-formed steel building during construction and earthquake testing." *Earthquake Eng. Struct. Dyn.* 49 (14): 1539–1558. https://doi.org/10.1002/eqe.3316.

Wang, X., and T. C. Hutchinson. 2021. "Earthquake and post-earthquake fire testing of a mid-rise cold-formed steel framed building. II: Shear wall behavior of design implications." *J. Struct. Eng.* 147 (9): 04021126. https://doi.org/10.1061/(ASCE)ST.1943-541X.0003098.

Wang, X., T. C. Hutchinson, G. Hegemeir, S. Gunisetty, P. Kamath, and B. Meacham. 2016. *Earthquake and post-earthquake fire performance of a mid-rise cold-formed steel framed building—Test program and test results. Final Report (CFS Test Program Report #2). Structural Systems Research Project*. Rep. No. SSRP-16/08. La Jolla, CA: Univ. of California, San Diego.

Wang, X., C. E. Wittich, T. C. Hutchinson, Y. Bock, D. Goldberg, E. Lo, and F. Kuester. 2020. "Methodology and validation of UAV-based video analysis approach for tracking earthquake-induced building displacements." *J. Comput. Civ. Eng.* 34 (6): 04020045. https://doi.org/10.1061/(ASCE)CP.1943-5487.0000928.

Wang, X., and J. Ye. 2016. "Cyclic testing of two-and three-story CFS shear-walls with reinforced end studs." *J. Constr. Steel Res.* 121 (Jun): 13–28. https://doi.org/10.1016/j.jcsr.2015.12.028.

Yu, C. 2010. "Shear resistance of cold-formed steel framed shear walls with 0.686 mm, 0.762 mm, and 0.838 mm steel sheet sheathing." *Eng. Struct.* 32 (6): 1522–1529. https://doi.org/10.1016/j.engstruct.2010.01.029.

Zhang, W., M. Mahdavian, Y. Li, and C. Yu. 2016. "Experiments and simulations of cold-formed steel wall assemblies using corrugated steel sheathing subjected to shear and gravity loads." *J. Struct. Eng.* 143 (4): 04016193. https://doi.org/10.1061/(ASCE)ST.1943-541X.0001681.

Zhang, W., M. Mahdavian, Y. Li, and C. Yu. 2017. "Seismic performance evaluation of cold-formed steel shear walls using corrugated steel sheathing." *J. Struct. Eng.* 143 (11): 04017151. https://doi.org/10.1061/(ASCE)ST.1943-541X.0001891.